

# Zinc Oxide Flower-Like Nanostructures That Exhibit Enhanced Toxicology Effects in Cancer Cells

Iêda M. M. Paino,<sup>\*,†</sup> Fernanda J. Gonçalves,<sup>‡</sup> Flavio L. Souza,<sup>‡</sup> and Valtencir Zucolotto<sup>†</sup>

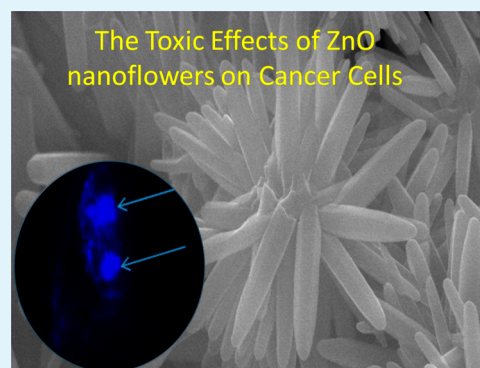
<sup>†</sup>Nanomedicine and Nanotoxicology Group, Physics Institute of São Carlos, University of São Paulo, São Carlos, São Paulo, Brazil

<sup>‡</sup>Federal University of ABC-UFABC, Santo André, São Paulo, Brazil

## Supporting Information

**ABSTRACT:** Nanostructured zinc oxide (ZnO) materials have been intensively studied because of their potential applications in cancer therapies. However, a better comprehension of the toxicity of the flower-like ZnO nanostructures toward cancer cells is still needed. In this study, we investigate the cytotoxicity of a ZnO flower-like nanostructure produced at low temperature via aqueous solution in human cervical carcinoma (HeLa) cells and noncancerous cell-line murine fibroblast (L929) cells. Nanotoxicology effects were analyzed to study apoptosis and necrosis processes, reactive oxygen species production, and cellular uptake. Cells remained incubated for 24 h in concentrations of 0.1, 1.0, and 10.0  $\mu\text{g mL}^{-1}$  ZnO nanoparticles (NPs), with the estimated rods length varying from  $1.7 \pm 0.4$  to  $2.3 \pm 0.4 \mu\text{m}$ , synthesized at different times (4, 2, and 0.5 h) by an aqueous solution method. The cytotoxic response observed in noncancerous and cancer cells showed that all of the ZnO NPs synthesized by an aqueous solution exhibited enhanced toxicology effects in cancer cells. ZnO flower-nanostructures exhibited a higher cytotoxic against cancer HeLa cells, in comparison to the noncancerous cell line L929. The cytotoxic response of ZnO NPs at 0.5, 2, and 4 h in L929 cells was not statistically significant. This ability may be of clinical interest because of the effectiveness of ZnO NPs to distinguish between normal and cancer cells in cancer therapy.

**KEYWORDS:** nanotoxicology, zinc oxide nanoparticles, human cervical cancer cell, fibroblast L929 cell, reactive oxygen species



## 1. INTRODUCTION

Nanomaterials based on transition-metal elements, such as zinc oxide (ZnO), have been considered potential candidates for medical applications. These nanomaterials are currently applied in industrial processes (such as textiles, antibacterial products, etc.) that are available for consumers.<sup>1,2</sup> Recently, Barui et al. (2012) studied the interaction of ZnO nanoflowers on the angiogenesis process.<sup>3</sup> The authors suggested that ZnO nanoflowers may be used as new therapeutic alternatives for cardiovascular and ischemic diseases exhibiting excellent proangiogenic activity, observed in vitro and in vivo.<sup>3</sup>

ZnO nanostructures have also been intensively investigated because of their intrinsic characteristics, which make them potential candidates for the treatment of different types of cancer.<sup>4</sup> However, both types of interactions that may occur between ZnO nanoparticles (NPs) and biological systems, as well as their possible toxicity, are unknown. There are very few studies conducted on the safety, toxicology, and exposure of ZnO NPs to normal and cancer cells. Indeed, the effects of these nanoscale materials on human health and the environment are not conclusive. Thus, a better comprehension regarding their use in cancer therapy and their potential toxicity is clearly needed.

The aqueous solution route is one of the most popular methods for ZnO NP preparation using zinc dichloride

( $\text{ZnCl}_2$ ), with the solution pH adjusted with  $\text{NH}_4\text{OH}$ , to synthesize one-dimensional ZnO powders or supported on transparent conductor substrates.<sup>5–10</sup> In a previous paper, a detailed contribution to the literature involving this method addressing the one-dimensional ZnO growth mechanism and its optical properties was carried out.<sup>9</sup> In agreement with the literature, it was found that the formation of ZnO using this methodology follows two main processes, in which the one at low temperature (below 100 °C) affects the rod length, whereas a competition between the rod growth and nucleation is reached from higher temperatures.<sup>11–13</sup> Because a few studies have reported the effects of ZnO flower-like nanostructures on cancer and noncancerous cells, this study was aimed at evaluating the toxicological effects of ZnO flower-like nanostructures on cervical carcinoma human (HeLa) and noncancerous fibroblast (L929) cells. Moreover, the present study intended to demystify the use of ZnO nanostructures for medical applications, showing that it can be used for cancer therapy without inducing serious damage to the noncancerous cells.

**Received:** September 21, 2016

**Accepted:** November 11, 2016

**Published:** November 23, 2016

## 2. EXPERIMENTAL SECTION

**2.1. Reagents and ZnO Synthesis.** All commercial chemicals were used as received, and all of the solutions were prepared using Millipore distilled water (18.2 M $\Omega$ -cm resistivity).

ZnO nanostructures were synthesized using an aqueous solution route under hydrothermal conditions at low temperature, as previously reported and detailed by Cunha and Souza (2013). Following a typical procedure, a solution containing 50 mmol L<sup>-1</sup> of ZnCl<sub>2</sub> (Carlo Erba Reagents, 97%) was synthesized by adding NH<sub>4</sub>OH (Vetec, 28–30%) under continuous stirring until the required pH 10.5 was reached for complete dissolution. The as-prepared solution was maintained at a constant temperature (90 °C) for different periods (0.5, 2, and 4 h). After each period, the solutions were quickly transferred to an ice bath to stop the kinetic reaction. Then the powders were washed by centrifugation and dried.

**2.2. Characterization.** The phase formation of all samples was evaluated via X-ray diffraction (XRD) measurements (Bruker D8 Focus) in the range of  $2\theta = 25\text{--}140^\circ$  using Cu K $\alpha$  radiation ( $\lambda = 1.5405 \text{ \AA}$ ) and a step size of  $0.02^\circ$ . The ZnO NP shape and size were investigated using scanning and transmission electron microscopies (SEM and TEM; FEI Company models Inspect F50 and Tecnai F20, 200 kV source). For the following characterizations, the samples were prepared as water dispersions with a concentration of 158 mg L<sup>-1</sup>.  $\zeta$  potential and dynamic light scattering (DLS) measurements were carried out for all samples. Electronic absorbance and photoluminescence (PL) spectroscopies were performed at 25 °C using a Varian Cary 50 Scan UV–vis spectrophotometer (tungsten lamp) and a Varian Cary Eclipse fluorescence spectrophotometer (xenon flash), respectively. Details on the optical characteristics of the ZnO materials are described elsewhere.<sup>9</sup> The  $\zeta$  potential and DLS were evaluated in a dispersion containing a cell culture medium (with additional 10% fetal bovine serum) and ZnO nanostructures at pH 7.2, using a Malvern Zetasizer Nano ZS equipment.

**2.3. HeLa and L929 Cell Culture.** All procedures for cell culture were conducted in a well-controlled environmental atmosphere to avoid endotoxin contamination. HeLa and L929 adherent cells were provided by the Federal University of Rio de Janeiro (cell bank of the UFRJ), Rio de Janeiro, Brazil. The cells were subcultured in 75 cm<sup>2</sup> flasks (TPP, Trasadingen, Switzerland) in Dulbecco's modified Eagle medium (DMEM; Vitrocell, São Paulo, Brazil). Cells were maintained in the presence of L-glutamine (2 mmol L<sup>-1</sup>) and penicillin/streptomycin (100 IU mL<sup>-1</sup>) with the addition of fetal bovine serum (FBS; 10%, Vitrocell). The cells remained in the appropriate conditions at constant temperature (37 °C) in an atmosphere of 5% CO<sub>2</sub> (Thermo Electron Co. incubator). The cell morphology was analyzed using an inverted microscope coupled to a Nikon camera (Nikon Eclipse Ti, Tokyo, Japan). Stock solutions of the NPs were sterilized to avoid contamination and prepared as previously mentioned using DMEM with 10% FBS in a sterile atmosphere immediately before cell incubation (item 2.4). The number of viable cells before each experiment was evaluated using trypan blue dye (Sigma-Aldrich, USA).<sup>14</sup> The number of viable cells incubated before each assay was 99% (data not shown).

**2.4. Incubation of the Cells with ZnO NPs.** To investigate the in vitro toxicity of ZnO nanoflowers, HeLa and L929 cells were incubated with 0.1, 1.0, and 10.0  $\mu\text{g mL}^{-1}$  ZnO NP for 24 h at 37 °C in 5% CO<sub>2</sub>. Negative control experiments containing only cells without ZnO NP were also performed. Positive control without ZnO NPs containing only cells with doxorubicin (Pharmacia & Upjohn, Italy) was analyzed.

**2.5. Flow Cytometry Assays.** The percentage of positive cells for fluorescence in apoptosis and necrosis was analyzed using the FACSCalibur flow cytometry (BD Biosciences, San Jose, CA) with BD Cell Quest software. The recommended experimental procedures were performed daily by using BD Calibryte (BD Biosciences) to guarantee flow cytometry calibration.

**2.6. Cytotoxicity Assays: Apoptosis and Necrosis.** HeLa and L929 cells ( $1 \times 10^6$  cells mL<sup>-1</sup>) in the presence of ZnO NPs were placed onto individual plates (TPP). The samples were then collected

and washed twice with a cold sterile buffer. Apoptosis and necrosis were determined by flow cytometry after staining with Annexin V-FITC/propidium iodide (PI; Annexin V-FITC apoptosis kit, Becton Dickinson, BD Biosciences, San Jose, CA) according to the instructions provided by the provider company. They were analyzed by 10000 events per experiment as percentages of positive cells.

**2.6.1. Hoechst Staining.** Imaging of the cell nucleus was performed using the Hoechst 33342 dye (Sigma-Aldrich, USA) to analyze the apoptotic nuclear morphology. The cells were fixed using 4% paraformaldehyde for 30 min, washed, and stained using Hoechst 33342 (2  $\mu\text{g mL}^{-1}$ ). The cell morphology was analyzed using confocal fluorescence microscopy (Zeiss LSM 780 confocal microscope).

**2.7. Reactive Oxygen Species (ROS) Intracellular Generation.** HeLa and L929 cells were treated with three different concentrations, as described in section 2.4, and under the same conditions. The negative control group was also evaluated without ZnO NP. After 24 h of NP exposure, cells were incubated in the presence of 10  $\mu\text{M}$  nonfluorescent 2,7'-dichlorodihydrofluorescein diacetate (DCFH-DA; Sigma-Aldrich, USA) for 1 h at 37 °C. DCFH-DA is converted into a fluorescent 2,7'-dichlorodihydrofluorescein (DCF) molecule upon ROS generation. Fluorescent ROS intracellular generation by ZnO NP (tests) and H<sub>2</sub>O<sub>2</sub> (positive control) was investigated using a FACSCalibur flow cytometer taking 10000 cells per sample.

**2.8. Cell Uptake.** The cellular uptake of ZnO NPs was also studied by side-scattered light (SSC) flow cytometry<sup>15</sup> using a FACSCalibur flow cytometer (Becton Dickinson, San Jose, CA).

**2.9. Statistical Analysis.** Data are expressed as the mean  $\pm$  standard deviation (SD) of at least three independent assays. GraphPad Prism 5.01 software was used for statistical analyses. The differences between the ZnO NP-treated samples and the controls were analyzed by one-way analysis of variance (ANOVA) followed by the posthoc Tukey test.  $p < 0.05$  was considered to be statistically significant.

## 3. RESULTS

The fundamental studies to evaluate the characteristics of the synthesized ZnO nanostructure were carried out before this analysis was submitted for toxicology analysis.

**3.1. Structural and Morphology Properties.** Figure 1 illustrates the XRD patterns for ZnO NPs, from which only a

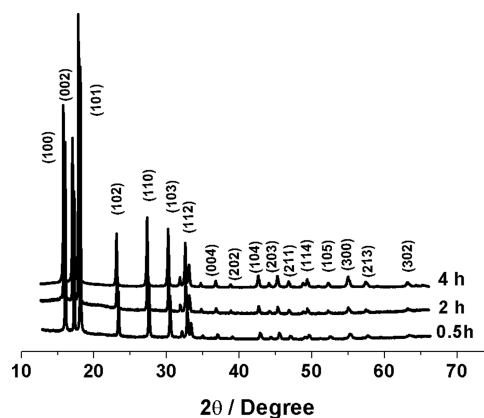


**Figure 1.** XRD patterns for all images of ZnO nanostructures synthesized by the aqueous solution route under hydrothermal conditions at 90 °C at different times for 0.5, 2.0, and 4.0 h.

bare ZnO phase is identified. XRD patterns were analyzed using the standard ZnO catalog no. 36-1451 as the reference. The latter analyses indicated that the synthetic chemical route used was efficient to produce metal oxide nanostructures at low temperature without further treatment. The lattice parameters for ZnO NPs were determined from the experimental data

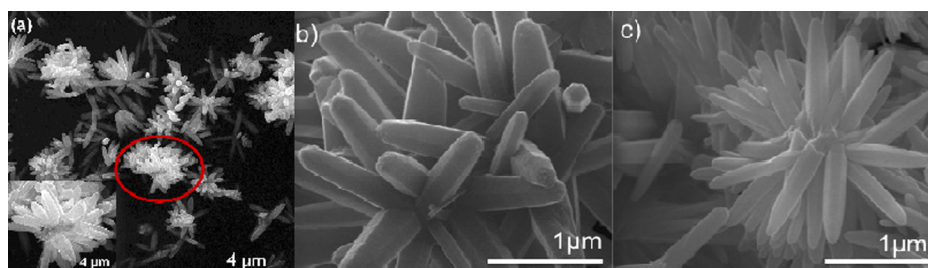


**Figure 2.** Field-emission SEM images of ZnO nanostructures synthesized by an aqueous solution route under hydrothermal conditions at 90 °C for (a) 0.5 h, (b) 2 h, and (c) 4 h.

**Table 1.**  $\zeta$  Potential and Hydrodynamic Diameter As Prepared and in a Cell Culture Medium Containing 10% FBS<sup>a</sup>

NPs	$\zeta$ potential (mV) as prepared in water	$\zeta$ potential (mV) in a cell culture medium containing 10% FBS	hydrodynamic diameter (nm) as prepared in water	hydrodynamic diameter (nm) in a cell culture medium containing 10% FBS
ZnO NP (4 h)	+27.4	-8.44 ± 1.9	1.4 ± 0.6	7.53 ± 1.3
ZnO NP (2 h)	+28.4	-8.94 ± 0.1	1.0 ± 0.6	7.61 ± 1.6
ZnO NP (0.5 h)	+26.0	-6.46 ± 0.51	0.9 ± 0.5	8.72 ± 2.0

<sup>a</sup>The data are reported as mean ± SD of quadruplicate experiments.

depicted in Figure 1. The estimated cell parameters ( $a \sim 3.249 \pm 0.003$  and  $c \sim 5.207 \pm 0.005$ ) and volumes ( $v \sim 47.59 \pm 0.01$ ) for all samples confirmed the formation of bare ZnO. No significant effect of the synthesis time on the lattice parameters was observed, in agreement with previous papers.<sup>16</sup>

ZnO morphology evolution was analyzed by SEM. Top-view SEM images exhibited in Figure 2 illustrate the formation of nanostructures with flower shape, which is expected for synthetic routes in which the precursor solution has its pH adjusted to  $\sim 10.5$ .<sup>9,10</sup> SEM images of the ZnO NPs obtained at different periods show flowers composed of rodlike hexagons on the top face (Figure 2a–c). The rod length was statistically determined from  $2.3 \pm 0.4$  to  $1.7 \pm 0.4 \mu\text{m}$ , respectively, using Image J (free software). The average rod diameter was estimated at 250 nm for all samples. The mechanisms and parameters that control the formation of ZnO NP with a flower shape had been the subject of recent investigations.<sup>9,10</sup>

**3.2. Optical Analysis.** The electronic transition spectra of all ZnO NPs exhibited a well-defined band between 360 and 390 nm. This band is related to the ZnO NP optical band gap, which can be affected by the presence of different particle sizes.<sup>13</sup> Optical band-gap energies between 3.18 and 3.20 eV were estimated using the experimental data illustrated in Figure 1Sa (Supporting Information). As observed in Figure 1Sb (Supporting Information), the PL measurements revealed a UV emission band at around 390 nm, and two additional bands in the visible range from 544 to 620 nm.<sup>17</sup> The presence of additional emission bands observed in the ZnO NP PL spectra is often related to the NP shape, size, and native defects.<sup>18–21</sup>

The presence of native defects and several morphologies were intensively investigated in the literature, which is commonly attributed to the synthetic procedure conditions.<sup>6,9,11,17</sup> A detailed investigation on the optical characterization of ZnO NPs obtained using the synthetic routes employed here was carried out by Cunha and Souza (2013),<sup>9</sup> revealing that different ZnO nanostructures can be designed upon adjustment of the synthesis time and temperatures. This is not the purpose of the present study; however, because the ZnO NP was pointed out as a potential candidate to kill cancerous cells, an

interesting research could be focused on evaluating the impact of the different morphologies, dimensions, and presence of defects on the health (toxicology effects).

**3.3. Size Distribution of the Nanoflowers.** Table 1 illustrates the ZnO NP hydrodynamic diameter and charge ( $\zeta$  potential) values determined before and after their addition to the cell culture medium (containing 10% FBS). The hydrodynamic diameters are shown in the Supporting Information (Figure 2S).

The cell uptake was analyzed by the SSC flow cytometry tool, as shown in Table 2. The SSC intensity measurement in

**Table 2.** Cellular Uptake by SSC Flow Cytometry Assessments after 24 h of Incubation<sup>a</sup>

treatment ( $10.0 \mu\text{g mL}^{-1}$ )	% SSC	
	HeLa cancer cell	L929 fibroblast cell
negative control	100.0 ± 0.0	100.0 ± 0.0
ZnO NP (4 h)	154.2 ± 0.9 <sup>b,c</sup>	105.0 ± 1.7
ZnO NP (2 h)	154.7 ± 0.1 <sup>b,d</sup>	111.2 ± 0.1 <sup>b</sup>
ZnO NP (0.5 h)	164.2 ± 2.5 <sup>b</sup>	109.1 ± 3.8 <sup>b</sup>

<sup>a</sup>The data are reported as mean ± SD of triplicate experiments. The negative control % SSC was considered as 100%. <sup>b</sup>Statistically different from the negative control group (ANOVA, Tukey's Multiple Comparison Test;  $p < 0.05$ ). <sup>c</sup>Statistically different ZnO NP 4 h versus ZnO NP 30 min group in a HeLa cell (ANOVA, Tukey's Multiple Comparison Test;  $p < 0.05$ ). <sup>d</sup>Statistically different ZnO NP 2 h versus ZnO NP 30 min group in a HeLa cell (ANOVA, Tukey's Multiple Comparison Test;  $p < 0.05$ ).

HeLa and L929 cells was statistically significant ( $p < 0.05$ ) at  $10.0 \mu\text{g mL}^{-1}$  (Table 2). The results from the SSC intensity showed that the HeLa cell uptake was higher than that in the L929 cells.

Apoptosis (Figure 3) and necrosis (Figure 4) in HeLa cells induced by ZnO NPs synthesized at 90 °C for different reaction times (0.5, 2, and 4 h) showed a significant toxicity ( $p < 0.05$ ). The increase was approximately 30% for apoptosis to NPs synthesized for 2 and 4 h ( $1.0$  and  $10.0 \mu\text{g mL}^{-1}$ ) and 50% for necrosis in HeLa cells at all concentrations in comparison to

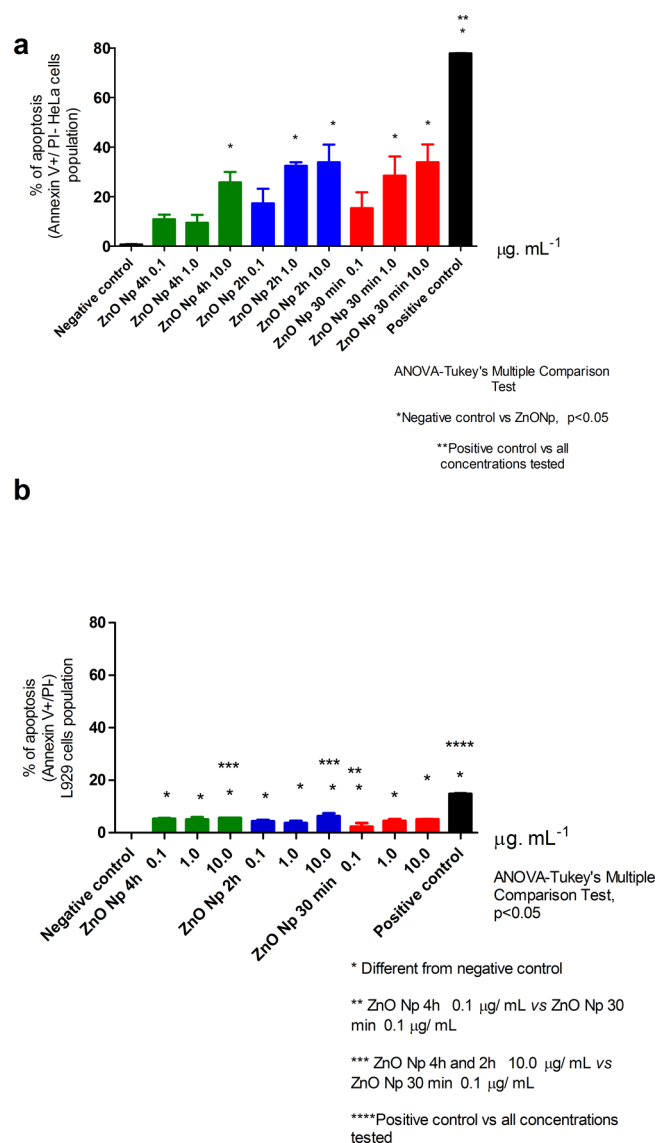


**Figure 3.** Effects of ZnO NPs on the percentage of apoptosis in HeLa (a) and L929 (b) cells. The data are reported as mean  $\pm$  SD. \*Statistically different from the negative control group (ANOVA, Tukey's Multiple Comparison Test;  $p < 0.05$ ).

negative control, after 24 h of exposure (Figures 3a and 4a, respectively). No apoptosis was induced in HeLa cells by ZnO NPs synthesized for 4 h at 0.1 and 1.0  $\mu\text{g mL}^{-1}$ , synthesized for 2 h at 0.1  $\mu\text{g mL}^{-1}$ , and synthesized for 0.5 h at 1.0  $\mu\text{g mL}^{-1}$ . In L929 cells, the apoptosis and necrosis processes were significant ( $p < 0.05$ ) for all samples tested (Figures 3b and 4b, respectively). However, apoptosis and necrosis were almost 10 times higher in the HeLa cells (Figures 3a and 4a, respectively) than in the L929 cells (Figures 3b and 4b, respectively). Apoptosis was further confirmed by fluorescence microscopy. Image analysis of the nucleus showed the control and cells–ZnO nanostructures using Hoechst 33342 staining (Figure 5). This analysis revealed important properties of the nucleus: the control cells exhibited spherical and homogeneous nuclei (Figure 5a), whereas the cells treated with ZnO nanoflowers (10  $\mu\text{g mL}^{-1}$  concentration and incubated for 24 h) showed characteristics of apoptosis, such as chromatin condensation in apoptotic cells and apoptotic bodies (Figure 5b–d).

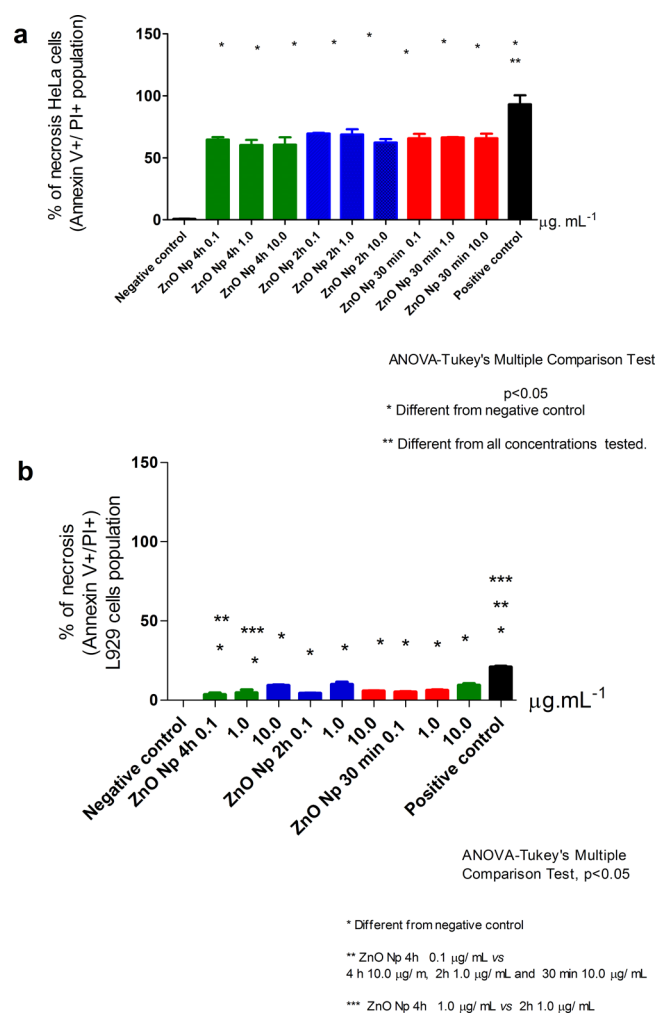


**Figure 4.** Effects of ZnO NPs on the percentage of necrosis in HeLa (a) and L929 (b) cells. The data are reported as mean  $\pm$  SD. \*Statistically different from the negative control group (ANOVA, Tukey's Multiple Comparison Test;  $p < 0.05$ ).

To confirm the potential of the ZnO NPs to cause oxidative stress in HeLa and L929 cells, the percentages of ROS production were investigated (parts a and b of Figure 6, respectively). These results were statistically significant ( $p < 0.05$ ) for all concentrations from the three ZnO NPs tested in both cells, in comparison to the negative control group.

#### 4. DISCUSSION

The mechanism and influence of the temperature and pH in the formation of ZnO nanoflowers will not be addressed in the present paper, but details about the synthesis condition can be found in work by Cunha and Souza (2013).<sup>9</sup> From the absorbance (Figure 1Sa) and PL (Figure 1Sb) spectra, the band-gap energies were determined in the range from 3.18 to 3.20 eV for all ZnO NPs. For ZnO NPs synthesized for 2 and 4 h under hydrothermal conditions, the band-gap energy was 3.2 eV, which represents the value reported for standard ZnO crystals. These results show that the synthetic method used here provided high-quality ZnO NPs obtained at temperatures below 100  $^{\circ}\text{C}$  and at relatively short synthetic times.<sup>22</sup>

The other parameter investigated here and affected by the ZnO nanoflower morphology and size was the hydrodynamic diameter ( $D_h$ ) because  $D_h$  is estimated by DLS following the

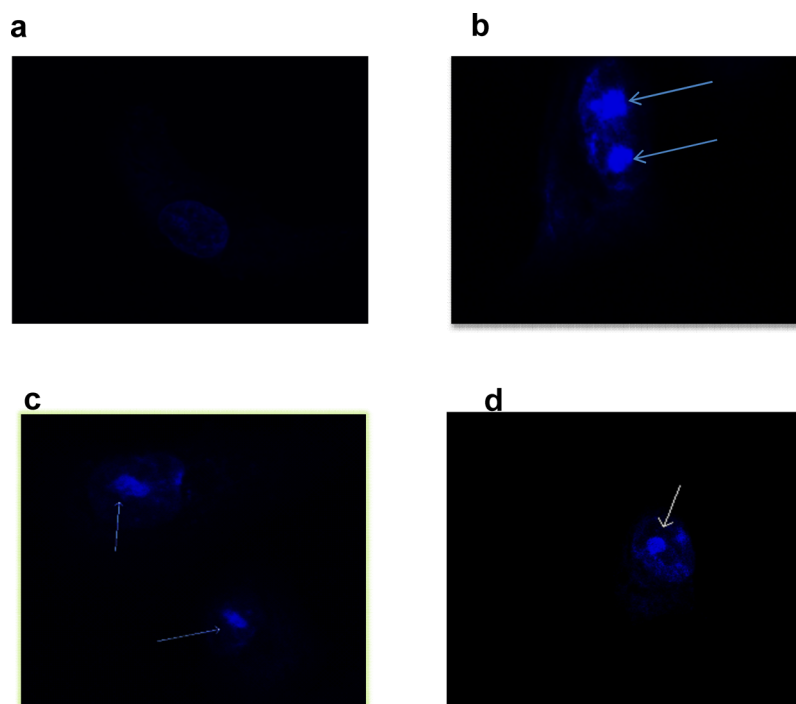


**Figure 5.** Confocal fluorescent images of HeLa cells stained with Hoechst 33342: (a) negative control. ZnO nanostructure-treated cells at  $10 \mu\text{g mL}^{-1}$  showing apoptotic cells with condensed or fragmented nuclei (indicated by arrows) synthesized at (b) 0.5 h, (c) 2 h, and (d) 4 h.

Stokes–Einstein equation, which has a close relationship to the hard sphere and liquid adherence on its surface. The high surface area due to longer rod length observed by samples prepared in 0.5 h could support the bigger  $D_h$  found because of their higher area for dipole interaction and light scattering. Indeed, the exponential decay is closely related to the particle size, which correlates a fast decay with smaller particles. Herein the nanoflower size/diameter is smaller for increasing synthesis times (0.5–6 h; see work by Cunha and Souza, 2013,<sup>9</sup> for synthesis details). At longer periods of synthesis from 2 to 6 h under hydrothermal conditions at constant temperature, a competition between nucleation and redissolution processes takes place favoring the size reduction and rod maturation. This could explain the smaller rod lengths observed in SEM images for ZnO NP samples prepared from 2 to 4 h in comparison with those prepared at 0.5 h. If the precursor solution remains under hydrothermal conditions for longer periods, viz., over 6 h, the nucleation process could become predominant again, increasing the rod length and favoring different rod top-face formations.

Hydrodynamic diameter and  $\zeta$  potential measurements were performed for ZnO nanostructures before and after incubation in a cell culture medium, as described in section 2.4. The results are shown in Table 1. It is known that the proteins present on FBS may strongly adsorb on the NPs, therefore stabilizing the suspensions and preventing aggregation, due to the so-called Corona phenomena.<sup>23</sup> In our studies, alterations of the  $\zeta$  potential and hydrodynamic diameter of ZnO NPs caused by FBS are shown in Table 1.

Data from the literature regarding the toxicology effects of ZnO NPs have increased substantially. However, the comparison between cancer and normal responses induced by ZnO NP-like nanoflowers synthesized at low temperatures via an aqueous solution or its interaction with cancer cells remains poorly explored. In this study, we advanced in this topic, upon

investigating the *in vitro* toxic impact of ZnO NPs on HeLa and L929 cells (Figures 3 and 4). The key parameter that could determine the difference in the results observed here is the synthesis time because it enables us to control the overall size of the nanostructure. When the precursor solution is subjected to a hydrothermal condition at temperature higher than  $85 \text{ }^\circ\text{C}$ , a supersaturation level is reached favoring nuclei formation in a basic pH. As a consequence, a rapid rodlike formation and maximum length growth is achieved in a short time, such as presented here (a maximum rod length after 0.5 min confirmed by the SEM images). The ZnO nanoflowers prepared at 2 h exhibited high surface area available for biological interactions and chemical reactions, which could enhance their toxicological effects and ability to kill cancer cells.

To demonstrate the cellular uptake of ZnO NP, the SSC with and without NPs was also studied.<sup>15</sup> ZnO NPs were more internalized in HeLa rather than in L929 cells, as shown in Table 2 ( $p < 0.05$ ). Cellular uptake demonstrated by SSC flow cytometry assessments (Table 2) showed that HeLa was capable of internalizing more efficiently ZnO NPs than L929 cells. Moreover, the internalization of ZnO NPs induced cell death through oxidative stress-dependent pathways (Figure 6a,b). NPs accumulating intracellular ROS may be an essential factor for necrosis. The decreased viability of cancer cells strongly suggests that oxidative stress, caused by ZnO NPs, resulted in cell death or apoptosis.

Recent evidence suggests that the cytotoxicity of ZnO NPs occurred through ROS and genotoxicity in cancer cells.<sup>23</sup> ROS production has been reported for a range of nanomaterials causing injury, which can be one of the primary mechanisms of toxicology effects for NPs.<sup>24–27</sup> Chandrasekaran and Pandurangan (2015)<sup>28</sup> showed that ZnO NPs exhibited more pronounced *in vitro* cytotoxic effects against C2C12 (cancer) than 3T3-L1 (normal fibroblast) cell lines, suggesting a selective antiproliferative effect.<sup>28</sup>

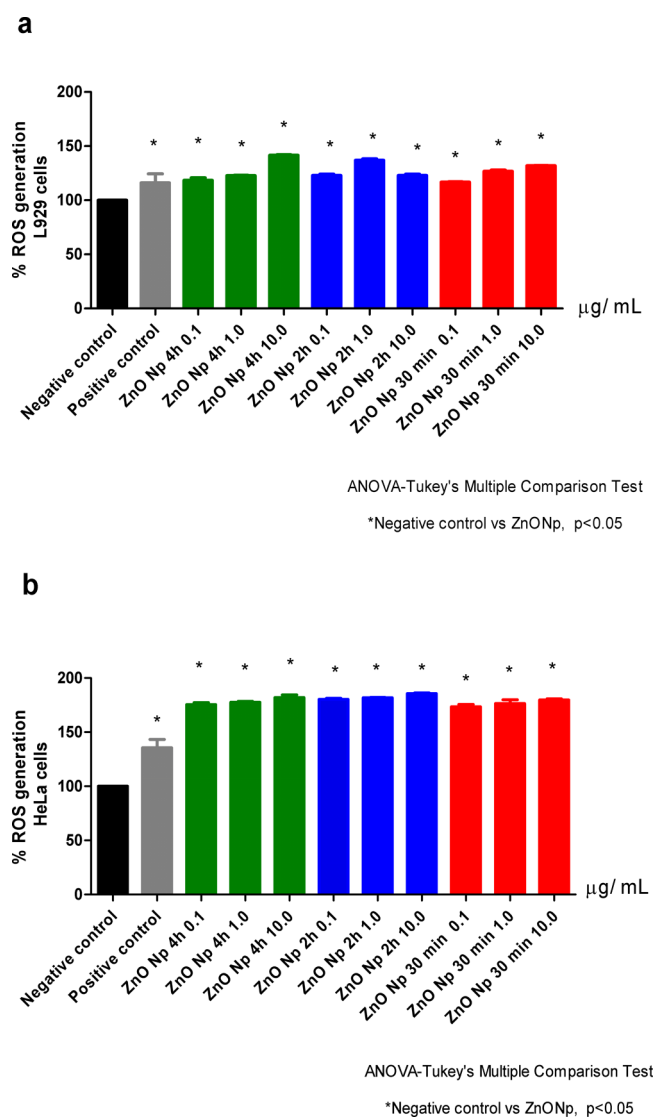


**Figure 6.** Effect of ZnO NPs on the generation of ROS in L929 (a) and HeLa (b) cells. The percentage of ROS generation of negative control was considered to be 100%. The data are reported as mean  $\pm$  SD. \*Statistically different from the negative control group (ANOVA, Tukey's Multiple Comparison Test;  $p < 0.05$ ).

In our study, as shown in Figures 3a and 4a, a dose-dependent significant increase in apoptosis and necrosis (approximately 30% and 80%, respectively) was observed in the HeLa cell, especially for ZnO NPs synthesized with a 2 h reaction time ( $p < 0.05$ ) at 1.0 and 10  $\mu\text{g mL}^{-1}$ . On the other hand, a slight and significant increase in apoptosis and necrosis (5% and 10%, respectively) was observed in L929 non-cancerous cells (Figures 3b and 4b, respectively). Similarly, significant and elevated levels of ROS production were observed in all concentrations in HeLa cells (approximately 80%; Figure 6b) compared to L929 cells (approximately 25%; Figure 6a). ZnO flower-like nanostructures exhibited a strong ability to damage cancer HeLa cells, in comparison to noncancerous L929 cells.

Cell death was induced by ZnO nanostructures, which can also be detected by morphological features. Apoptosis is probably the mechanism responsible for cell death through excessive ROS generation. The cell morphology was evaluated to confirm that ZnO nanostructure caused cell death through

an apoptotic process with ROS generation. The nuclear fragmentation and condensation visualized with Hoechst 33342 staining provided additional evidence of apoptosis.

Taken together, data from the present study demonstrated that ZnO nanostructures produced at a 2 h reaction time induced ROS generation, leading to toxicology effects in HeLa cancer and L929 noncancerous cells. Probably, this intracellular signaling pathway may be responsible for apoptosis or cell death. ZnO nanostructures exhibited a preferential ability to kill cancer cells in comparison to noncancerous cells.

## 5. CONCLUSION

In conclusion, our data demonstrated that the use of increased doses (0.1, 1.0, and 10.0  $\mu\text{g mL}^{-1}$ ) of ZnO NPs induced higher levels of apoptosis and necrosis in HeLa cancer cells, in comparison to the ones observed for noncancerous L929 cells. We have shown that the decrease in the cell viability was due to the induction of oxidative stress responses. This ability may be of clinical interest, as in cancer therapy. Our results pointed to the selective ability exhibited by the ZnO nanostructures to induce more pronounced toxic effects in cancer cells, in comparison to noncancerous cells, which may shed light in this field, demystifying the use of oxide NPs in medical applications, with reduced side effects to normal cells.

## ASSOCIATED CONTENT

### Supporting Information

The Supporting Information is available free of charge on the ACS Publications website at DOI: 10.1021/acsami.6b11950.

UV-vis wavelength (a) and PL emission spectra (b) in water of ZnO nanostructures grown in solution at different reaction times (Figure S1) and hydrodynamic diameters measured after ZnO NPs (10.0  $\mu\text{g mL}^{-1}$ ) dilution into a cell culture medium supplemented with serum (10% FBS) synthesized at 0.5, 2, and 4 h (Figure S2) (PDF)

## AUTHOR INFORMATION

### Corresponding Author

\*Phone: +55 16 3373 9875. E-mail: [iedamp@hotmail.com](mailto:iedamp@hotmail.com).

### ORCID

Iêda M. M. Paino: 0000-0002-6886-8901

### Notes

The authors declare no competing financial interest.

## ACKNOWLEDGMENTS

The authors are thankful for funding provided by Brazilian sponsors. We acknowledge financial support from CAPES-PNPD (Grant 23038.007902/2010-25) and CNPq (Grants 473669/2012-9 and 552127/2011-6). F.L.S. is grateful to FAPESP (Grant 2011/19924-2).

## REFERENCES

- (1) Nounou, H.; Attia, M.; Shalaby, M.; Arafah, M. Oral Exposure to Zinc Oxide Nanoparticles Induced Oxidative Damage, Inflammation And Genotoxicity In Rat's Lung. *Life Sci. J.* **2013**, *10*, 1969–1979.
- (2) Musee, N.; Thwala, M.; Nota, N. The Antibacterial Effects of Engineered Nanomaterials: Implications For Wastewater Treatment Plants. *J. Environ. Monit.* **2011**, *13*, 1164–1183.
- (3) Barui, A. K.; Veeriah, V.; Mukherjee, S.; Manna, J.; Patel, A. K.; Patra, S.; Pal, K.; Murali, S.; Rana, R. K.; Chatterjee, S.; Patra, C. R.

Zinc Oxide Nanoflowers Make New Blood Vessels. *Nanoscale* **2012**, *4*, 7861–7869.

(4) Rasmussen, J. W.; Martinez, E.; Louka, P.; Wingett, D. G. Zinc Oxide Nanoparticles For Selective Destruction Of Tumor Cells And Potential For Drug Delivery Applications. *Expert Opin. Drug Delivery* **2010**, *7*, 1063–1077.

(5) Wang, J. X.; Sun, X. W.; Yang, Y.; Huang, H.; Lee, Y. C.; Tan, O. K.; Vayssieres, L. Hydrothermally Grown Oriented ZnO Nanorod Arrays For Gas Sensing Applications. *Nanotechnology* **2006**, *17*, 4995–4998.

(6) Gu, C.; Huang, J.; Wu, Y.; Zhai, M.; Sun, Y.; Liu, J. Preparation Of Porous Flower-Like ZnO Nanostructures And Their Gas-Sensing Property. *J. Alloys Compd.* **2011**, *509*, 4499–4504.

(7) Vayssieres, L. An Aqueous Solution Approach To Advanced Metal Oxide Arrays On Substrates. *Appl. Phys. A: Mater. Sci. Process.* **2007**, *89*, 1–8.

(8) Vayssieres, L. Designing Ordered Nanoarrays From Aqueous Solutions. *Pure Appl. Chem.* **2006**, *78*, 1741–1747.

(9) Cunha, D. M.; Souza, F. L. Facile Synthetic Route For Producing One-Dimensional Zinc Oxide Nanoflowers And Characterization Of Their Optical Properties. *J. Alloys Compd.* **2013**, *577*, 158–164.

(10) Cunha, D. M.; Ito, N. M.; Xavier, A. M.; Arantes, J. T.; Souza, F. L. Zinc Oxide Flower-Like Synthesized Under Hydrothermal Conditions. *Thin Solid Films* **2013**, *537*, 97–101.

(11) Li, W. J.; Shi, E. W.; Zhong, W. Z.; Yin, Z. W. Growth Mechanism And Growth Habit Of Oxide Crystals. *J. Cryst. Growth* **1999**, *203*, 186–196.

(12) Zhang, J.; Sun, L. D.; Yin, J. L.; Su, H. L.; Liao, C. S.; Yan, C. H. Control of ZnO Morphology Via A Simple Solution Route. *Chem. Mater.* **2002**, *14*, 4172–4177.

(13) Lu, F.; Cai, W.; Zhang, Y. ZnO Hierarchical Micro/Nano-architectures: Solvothermal Synthesis And Structurally Enhanced Photocatalytic Performance. *Adv. Funct. Mater.* **2008**, *18*, 1047–1056.

(14) Freshney, R. I. *Culture of Animal Cells: A Manual of Basic Technique*; John Wiley & Sons Publications: New York, 2000.

(15) Suzuki, H.; Toyooka, T.; Ibuki, Y. Simple And Easy Method To Evaluate Uptake Potential Of Nanoparticles In Mammalian Cells Using A Flow Cytometric Light Scatter Analysis. *Environ. Sci. Technol.* **2007**, *41*, 3018–3024.

(16) Wang, R. C.; Liu, C. P.; Huang, J. L.; Chen, S. J. ZnO Symmetric Nanosheets Integrated With Nanowalls. *Appl. Phys. Lett.* **2005**, *87*, 87–95.

(17) Wen, F.; Li, W.; Moon, J. H.; Kim, J. H. Hydrothermal Synthesis Of ZnO: Zn With Green Emission At Low Temperature With Reduction Process. *Solid State Commun.* **2005**, *135*, 34–37.

(18) Huang, Y. H.; He, J.; Zhang, Y.; Dai, Y.; Gu, Y. S.; Wang, S.; Zhou, C. Morphology, Structures And Properties Of ZnO Nanobelts Fabricated By Zn-Powder Evaporation Without Catalyst At Lower Temperature. *J. Mater. Sci.* **2006**, *41*, 3057–3062.

(19) Xu, F.; Lu, Y.; Xie, Y.; Liu, Y. Synthesis and Photoluminescence of Assembly-Controlled ZnO Architectures by Aqueous Chemical Growth. *J. Phys. Chem. C* **2009**, *113*, 1052–1059.

(20) Yang, Q.; Tang, K.; Zuo, J.; Qian, Y. Synthesis and Luminescent Property of Single-Crystal ZnO nanobelts By A Simple Low Temperature Evaporation Route. *Appl. Phys. A: Mater. Sci. Process.* **2004**, *79*, 1847–1851.

(21) Yu, W.; Li, X.; Gao, X. Catalytic Synthesis and Structural Characteristics of High-Quality Tetrapod-Like ZnONanocrystals by a Modified Vapor Transport Process. *Cryst. Growth Des.* **2005**, *5*, 151–155.

(22) Zhou, Z.; Deng, Y. Kinetics Study of ZnONanorod Growth in Solution. *J. Phys. Chem. C* **2009**, *113*, 19853–19858.

(23) Fatissou, J. Physicochemical Characterization Of Engineered Nanoparticles Under Physiological Conditions: Effect Of Culture Media Components And Particle Surface Coating. *Colloids Surf, B* **2012**, *91*, 198–204.

(24) Wahab, R.; Siddiqui, M. A.; Saquib, Q.; Dwivedi, S.; Ahmad, J.; Musarrat, J.; Al-Khedhairi, A. A.; Shin, H. S. ZnO Nanoparticles Induced Oxidative Stress And Apoptosis In Hepg2 And MCF-7

Cancer Cells And Their Antibacterial Activity. *Colloids Surf, B* **2014**, *117*, 267–276.

(25) Nel, A.; Xia, T.; Madler, L.; Li, N. Toxic Potential Of Materials At The Nanolevel. *Science* **2006**, *311*, 622–627.

(26) Paino, I. M.; Marangoni, V. S.; de Oliveira, R. de C.; Antunes, L. M.; Zucolotto, V. Cyto And Genotoxicity Of Gold Nanoparticles In Human Hepatocellular Carcinoma and Peripheral Blood Mononuclear Cells. *Toxicol. Lett.* **2012**, *215*, 119–125.

(27) Paino, I. M.; Zucolotto, V. Poly (Vinyl Alcohol)-Coated Silver Nanoparticles: Activation Of Neutrophils and Nanotoxicology Effects In Human Hepatocarcinoma and Mononuclear Cells. *Environ. Toxicol. Pharmacol.* **2015**, *39*, 614–621.

(28) Chandrasekaran, M.; Pandurangan, M. In Vitro Selective Anti-Proliferative Effect Of Zinc Oxide Nanoparticles Against Co-Cultured C2C12 Myoblastoma Cancer and 3T3-L1 Normal Cells. *Biol. Trace Elem. Res.* **2016**, *172*, 148–154.